

Study of Long-Range Collisions and Wire Compensation for Tevatron Run-II

Frank Zimmermann, CERN, AB Department, 1211 Geneva 23, Switzerland

Tanaji Sen, Bela Erdelyi, Vinay Boochoa, FNAL, Batavia, IL 60510, USA

March 8, 2004

Abstract

This report summarizes studies of long-range collisions and their compensation by current-carrying wires for the Tevatron Run-II, which were performed during a two-week stay at Fermilab, February 22 to March 8, 2004. The weak-strong code WSDIFF was significantly extended to simulate the actual long-range encounters at the Tevatron for different antiproton bunches in the train at injection and in collision. Tune footprints and diffusive apertures simulated by this code are presented for various cases, differing in the bunch position, the energy, the number of long-range and head-on collisions, the presence of additional compensating wires and the momentum deviation. It is confirmed that the solution of 4 wires for injection, previously found by B. Erdelyi, raises the dynamic aperture, by about $1.0-1.5\sigma$. For both injection and collision an ideal compensation of the 6 or 3 closest long-range encounters was modeled, by removing these collisions altogether. At collision, an improvement in the dynamic aperture of the order of $0.5-1.0\sigma$ is found. The much more copious residual long-range collisions are shown to also strongly affect the diffusive aperture, however, which highlights a lack of correlation between dynamic aperture and tune footprints. The dynamic aperture widely varies with the bunch number, ranging from 5 to 8σ along the train, in collision for on-momentum particles. Analytical calculations of tune shift, coupling, chromaticity and chromatic coupling similarly reveal a large variation from bunch to bunch, amounting to 16 units in chromaticity and 4 or 5 units in chromatic coupling. Achieving compensation for all bunches in the train appears a non-trivial challenge for dc wires, in particular if off-energy is also to be corrected.

In a machine study on March 1, the Tevatron electron lens was used to simulate a wire and the dependences of beam lifetime, tune, emittances and bunch length on the beam-TEL distance were explored. The results of this experiment are reported elsewhere [1].

Overview

For a recent general review of beam-beam effects at the Tevatron Run-II see Ref. [2].

Here we simulate the dynamic aperture due to long-range collisions at injection for bunch A1 and in collisions for bunches A1, A6 and A12. We in particular explore how much the dynamic aperture improves, if the closest encounters are removed or, if, at injection, 4 wires are added with positions and settings as previously computed by B. Erdelyi. We compute tune footprints for all cases under study. In the attempt to identify a few “most harmful collisions”, we also map the LR encounters into the phase space at one location, and we investigate how tune shift, chromaticity, coupling and chromatic coupling due to long-range collisions build up around the ring. An analytical estimate of diffusion coefficients is described. Unfortunately we could not yet solve the related integrals for the 4-D case explicitly. The effects of momentum deviation, chromaticity and dispersive orbits at the long-range collisions are studied with an expanded version of WSDIFF [3].

We first discuss results at injection energy and then for collision. This is followed by a concluding summary. In the appendix we compile some analytical formulae.

Injection

We start by considering the situation at injection. Linear transfer matrices between all 72 collision points and also the rf cavity were provided by T. Sen, as were the proton beam sizes and the beam-beam separation in the two planes. Other proton beam parameters are listed in Table 1.

Table 1: Basic proton-beam parameters at injection

Parameter	Value
proton bunch intensity	2.7e11
95% emittance	20pi
tunes	20.582, 20.5704
circumference	6283.187 m
Energy	150 GeV

The beta functions at the starting point (1st parasitic collision) are 19.76 m and 19.52 m. The 1st parasitic (at injection, "cog 0" i.e before any cogging has occurred) for pbar bunch 1 is 5.646 m downstream of B0 in the pbar direction (bunch 1 stays longest at injection and suffers most from beam-beam). The separations that Tanaji Sen sent are the beam separations with respect to the protons. The total 1-turn matrix from the 1st parasitic encounter around the ring, without beam-beam effects, is

$$\begin{pmatrix} x \\ x' \\ y \\ y' \end{pmatrix}_{n+1} = \begin{pmatrix} 0.785 & -9.738 & 0 & 0 & 0.350 \\ 0.306 & -2.525 & 0 & 0 & 55.11 \\ 0 & 0 & 0.475 & -8.355 & 0.188 \\ 0 & 0 & 0.249 & -2.282 & 34.63 \end{pmatrix} \begin{pmatrix} x \\ x' \\ y \\ y' \\ \delta \end{pmatrix}_n.$$

The two pictures in Fig.1 show the image of all LRBB collisions mapped into the normalized phase space at the 1st parasitic collision point. The helical structure is clearly visible, appearing as a single circle in the horizontal projection and as a 'double-helix' in the vertical. We can also plot the normalized transverse distances to the origin for the two planes, as is illustrated in Figure 2. There are 6 encounters for which the normalized distance is less than 7σ . They are compiled in Table 2.

Table 2: LR encounters closest to the origin for bunch A1 at injection.

LR encounter no.	Normalized total distance [σ]
13	6.83
46	6.36
48	6.13
61	5.51
69	6.55
71	6.70

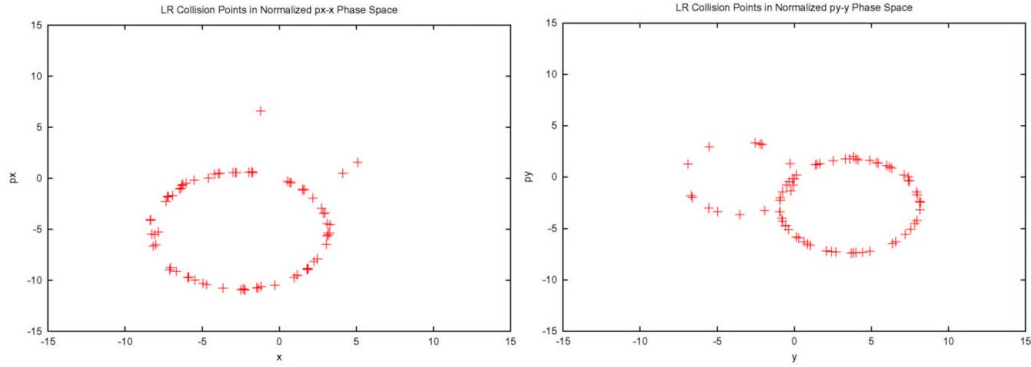


Figure 1: Image of all LRBB collisions mapped into the horizontal (left) and vertical (right) normalized phase space at the 1st parasitic collision point for bunch A1 at injection. The axes are in units of the rms beam size and rms divergence.

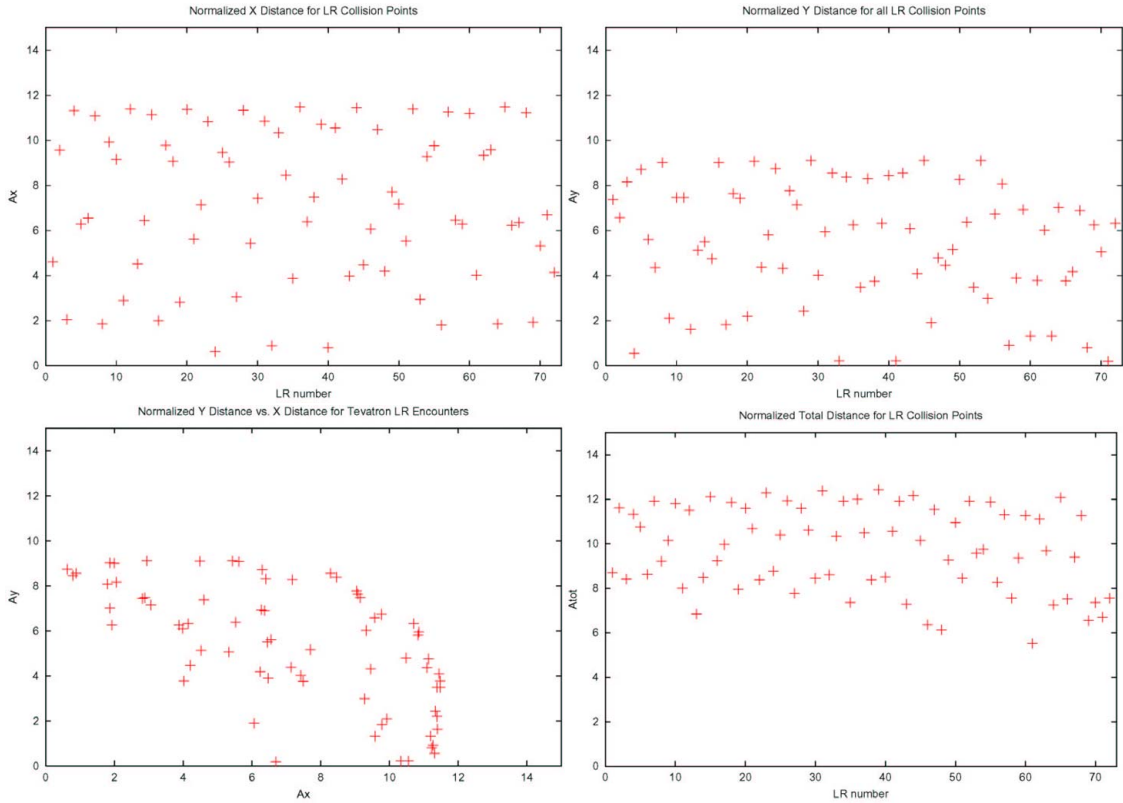


Figure 2: The normalized distances of the opposing beam to the origin in phase space in the horizontal and vertical plane as a function of LR encounter no. (top left and right), and against each other (bottom left), and the total distance to the origin, $A_{tot} = \sqrt{A_x^2 + A_y^2}$, for each collision point (bottom right), considering bunch A1 at injection.

For simulations we use an extension of the tracking program WSDIFF described in [3]. Figure 3 displays phase space plots for the two transverse planes as well as particle amplitudes as a function of time, for 15 trajectories with random initial conditions in the presence of all long-range encounters for bunch A1 at injection. The phase space looks diffuse, due to the strong coupling caused by the off-plane long-range collisions, but over this short time scale there is no noticeable growth in amplitude. The unpopulated ‘rings’ simply reflect the choice of initial conditions and have no deeper meaning.

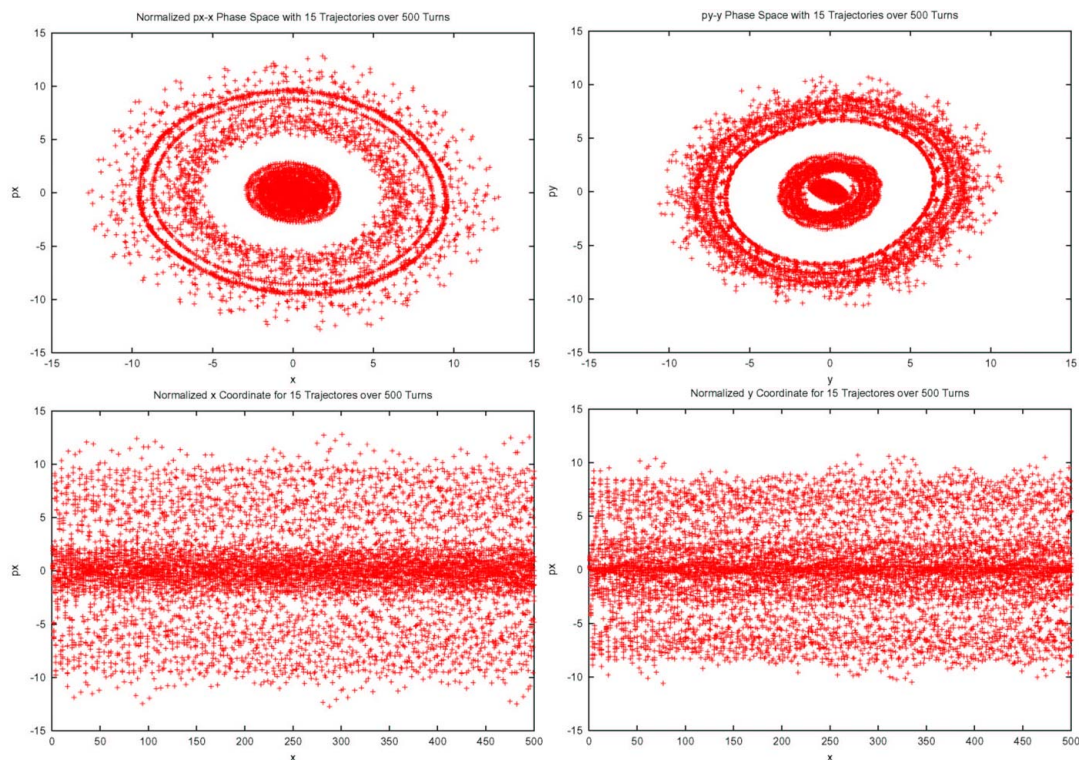


Figure 3: The normalized horizontal and vertical phase space (top row) and the normalized horizontal and vertical coordinates as a function of turn number (bottom row) for 15 trajectories with random start amplitudes between 0 and 10σ over 500 turns.

Figure 4 shows tune footprints computed with all and only a part of the long-range collisions. Some particles appear locked to the linear coupling resonance (which can be interpreted as an artifact of our peak finding algorithm for the FFT spectrum). The footprint does not noticeably change, if the 6 closest encounters are excluded (top right vs. top left picture). Comparison of the tune footprint from WSDIFF with that computed by T. Sen’s code BBSIM yields a satisfactory agreement (bottom picture).

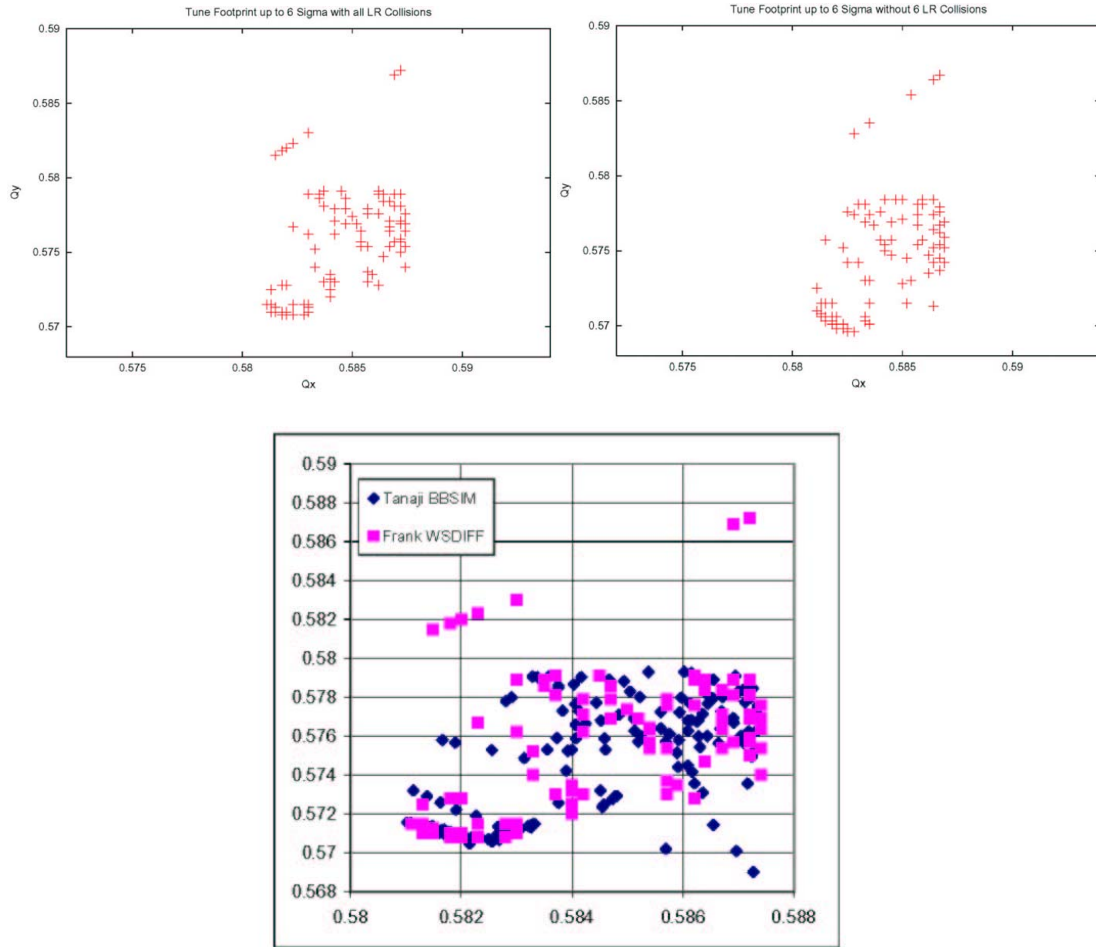


Figure 4: Tune footprint for start amplitudes up to 6σ in each plane with all LR encounters present (top left) and without the 6 closest (top right); comparison of the bare tune footprints with all long-range collisions computed by CERN code WSDIFF and by Tanaji Sen's code BBSIM (bottom).

We determine the strength of action diffusion as a function of start amplitude by launching groups of 100 or 169 particles with identical initial linear action values and random betatron phase and computing the growth in average action variance with time (the averaging is applied over 1000 turns to suppress short-time fluctuations caused by phase-space distortions). Figures 5 and 6 compare the result when all LR collisions are included with that obtained if the closest (most harmful?) encounters are removed, thus modeling their perfect compensation. The dynamic aperture with all long-range collisions is about 6σ in the horizontal diffusion and $4.5-5.0\sigma$ vertically. This would suggest that particles are lost preferentially in the vertical direction. The dynamic aperture is nearly unchanged, if the 6 closest encounters are excluded, except for a small improvement equal to, or less than, 0.5σ , vertically.

Table 3 lists analytical values of the linear tune shifts, chromaticities, coupling and chromatic coupling induced by all long-range collisions for bunch A1 at injection. The numbers are moderate, except perhaps the 1 unit in chromatic coupling that might be difficult to correct.

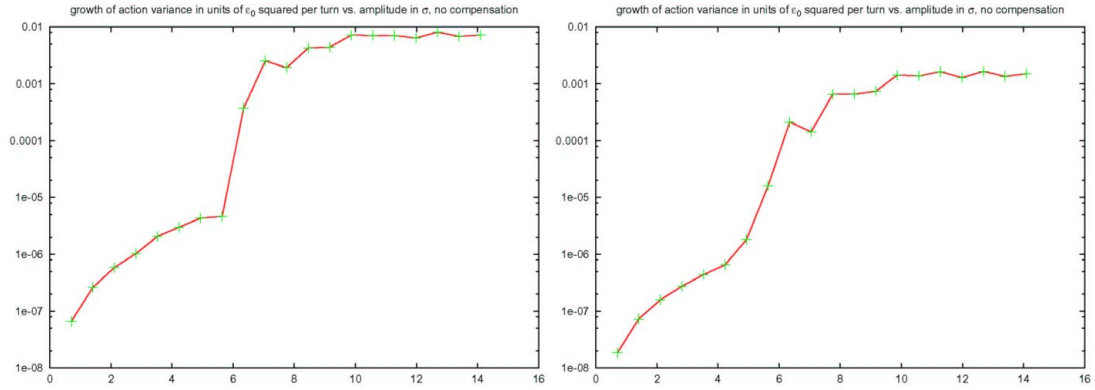


Figure 5: Slope of increase in horizontal (left) and vertical action variance (right) with time in units of the square of the nominal beam emittance per turn as a function of horizontal or vertical start amplitude in units of σ (the start amplitudes in the two planes are chosen equal), for bunch A1 at injection when all long-range collisions are present.

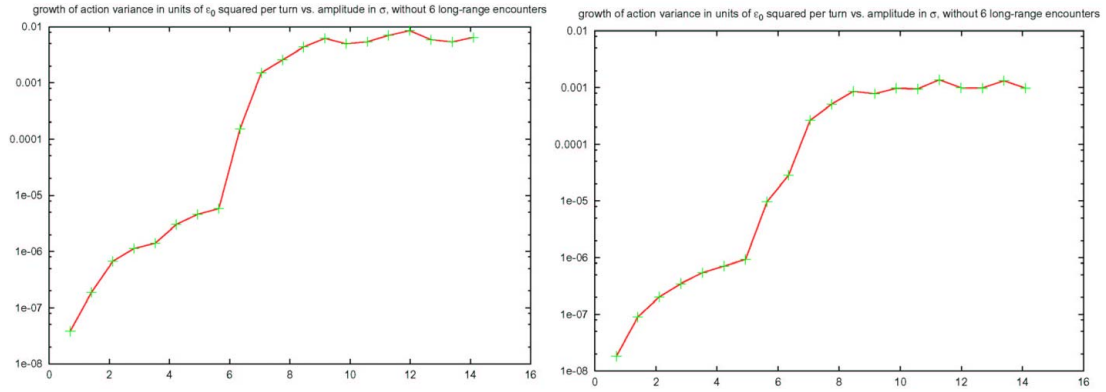


Figure 6: Slope of increase in horizontal (left) and vertical action variance (right) with time in units of the square of the nominal beam emittance per turn as a function of horizontal or vertical start amplitude in units of σ (the start amplitudes in the two planes are chosen equal), for bunch A1 at injection when the 6 closest long-range collisions are removed.

Table 3: Total tune shifts, chromaticities, coupling driving terms, and chromatic couplings induced by long-range collisions for pbar bunch A1 at injection.

Pbar bunch	A1
X Tune shift ΔQ_x	-0.00015
Y Tune shift ΔQ_y	0.0014
X Chromaticity Q'_x	0.28
Y Chromaticity Q'_y	0.56
Coupling real part $\text{Re}[\kappa]$	0.0029
Coupling imaginary part $\text{Im}[\kappa]$	-0.0014
Chromatic coupling $\text{Re}[d\kappa/d\delta]$	-1.33
Chromatic coupling $\text{Im}[d\kappa/d\delta]$	-0.027

We next explore the effect of the 4-wire compensation previously determined by B. Erdelyi and T. Sen. The wires and their parameters, as optimized by B. Erdelyi [4], are listed in Table 4. Figure 7 compares A1 tune footprints for the nominal situation with the case where the 4 wires are active. The wires seem to ‘rotate’ the footprint by about 90 degrees in phase space, without much effect on its overall extent.

Table 4: Parameters of 4 wires used for compensation at injection. The distance refers to the transverse position of the wire with respect to the pbar helical orbit.

Wire	position	index	X distance	Y distance	Current	Length
WA	825.557	10	9.981	-0.613	50 A	1 m
WF	2091.93	26	8.376	-5.463	232 A	1 m
WE	3126.49	40	14.935	10.046	-25 A	1 m
WC	5231.48	65	9.071	-9.071	75 A	1 m

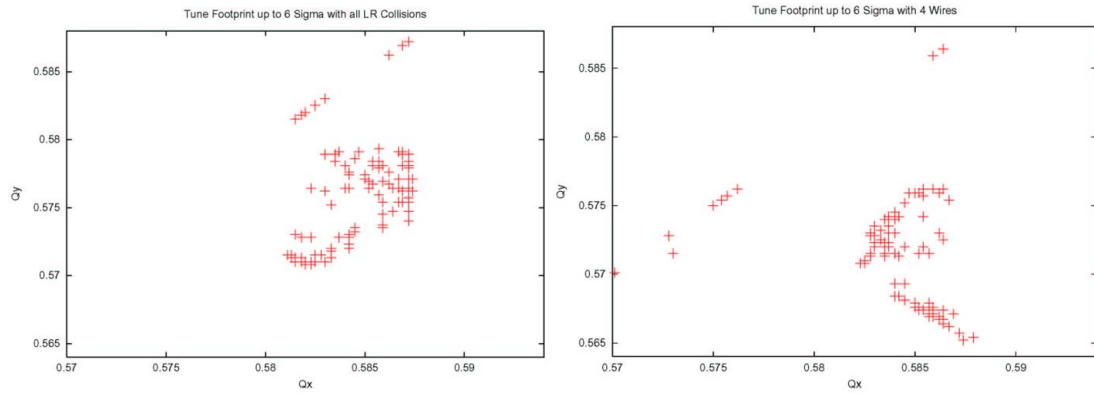


Figure 7: Tune footprints up to 7σ with all long-range collisions (left) and when the 4 wires are added (right).

Figure 8 presents diffusion rates for the case with all long-range encounters and the additional 4 wires for bunch A1. The left pictures refer again to the horizontal diffusion, the right ones to diffusion in the vertical plane. Only the scale of the horizontal axes is different for the top and bottom pictures. The dynamic aperture is again found at 6σ horizontally, but it now is 6σ as well in the vertical plane. Hence the wires improve the overall dynamic aperture (the minimum over the two planes) by about $1.0\text{-}1.5\sigma$. This is a better performance than obtained by removing the 6 innermost encounters!

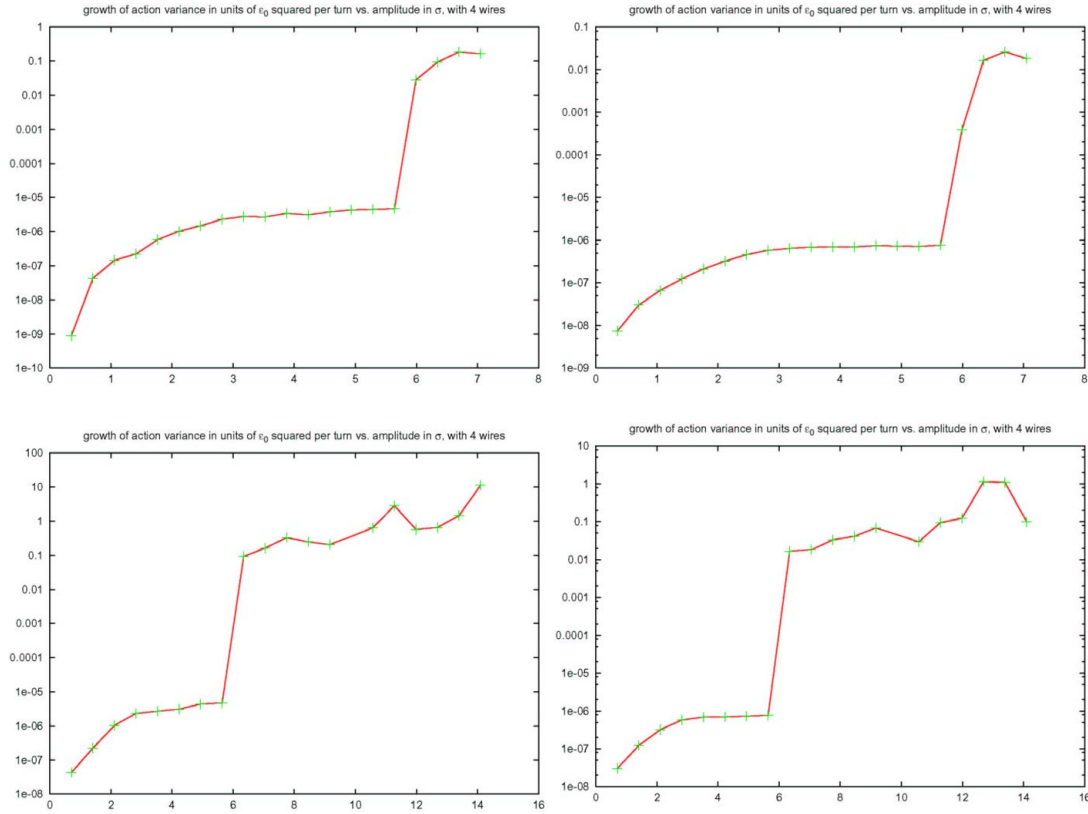


Figure 8: Slope of increase in horizontal (left) and vertical action variance (right) in time in units of the square of the nominal beam emittance per turn as a function of horizontal or vertical start amplitude in units of σ (the start amplitudes in the two planes are chosen equal), for bunch A1 at injection when the 4 wires are added. The top and bottom pictures differ in the horizontal scale.

Collision

We next look at collision, starting with bunch number A6 in collision, which is a typical bunch. Parameters in collision are listed in Table 5. The total 1-turn matrix from the end of the head-on collision in B0 once around the ring, without beam-beam effects, is

$$\begin{pmatrix} x \\ x' \\ y \\ y' \end{pmatrix}_{n+1} = \begin{pmatrix} -0.867 & -0.175 & 0 & 0 & 0.014 \\ 1.418 & -0.867 & 0 & 0 & 22.86 \\ 0 & 0 & -0.891 & -0.163 & 0.001 \\ 0 & 0 & 1.266 & -0.891 & -111.6 \end{pmatrix} \begin{pmatrix} x \\ x' \\ y \\ y' \\ \delta \end{pmatrix}_n.$$

Figure 9 shows the local beam sizes and beam-beam separations at all collision points for bunches A1, A6, and A12.

Table 5: Beam parameters in collision.

parameter	Value
proton bunch intensity	$2.7e11$
95% emittance	20π
pbar tunes	20.583, 20.575
circumference	6283.187 m
energy	980 GeV

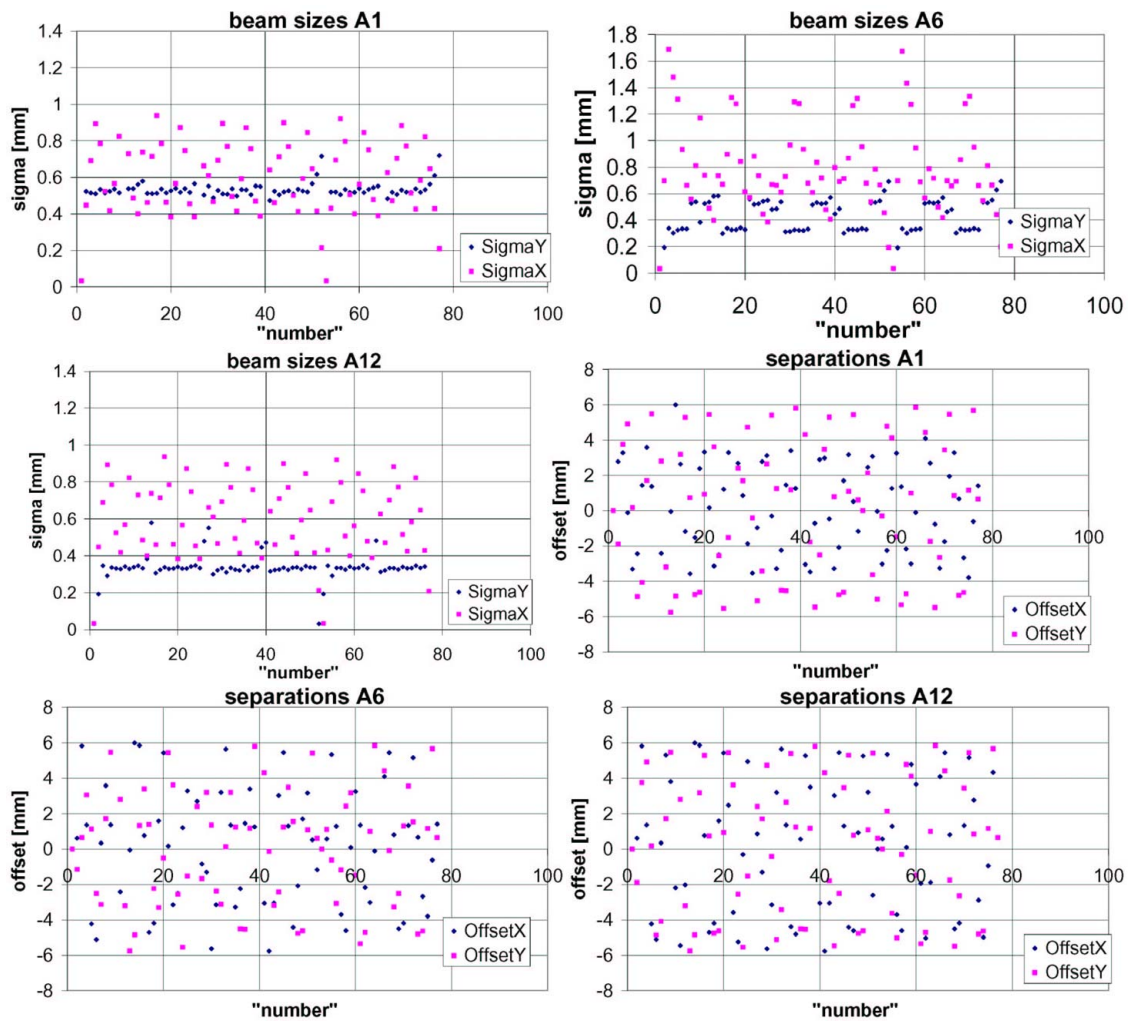


Figure 9: Rms proton beam sizes and beam-beam offsets at all 72 collision points for bunches A1, A6 and A12.

Figure 10 shows the mapping of all long-range encounters into the normalized phase space at the starting point (B0). It is surprising that the planes with a double-helix and with a single helix are interchanged compared with the case at injection (compare the two top pictures with Fig. 1). The amplitude of the helix is about 10σ , which is roughly 2σ larger than at injection. Note that dispersive contributions are not considered when

mapping the phase space. So the actual horizontal beam sizes at a particular long-range collision point may be larger than those used as normalizing unit here. The closest encounters are further and more distinctly separated from the rest than at injection. Only three collisions are found below 7σ . They are listed in Table 6.

Table 6: Closest long-range encounters (below 7σ) for bunch A6 in collision.

LR encounter no.	Normalized total distance [σ]
1	6.07
47	6.33
48	5.95

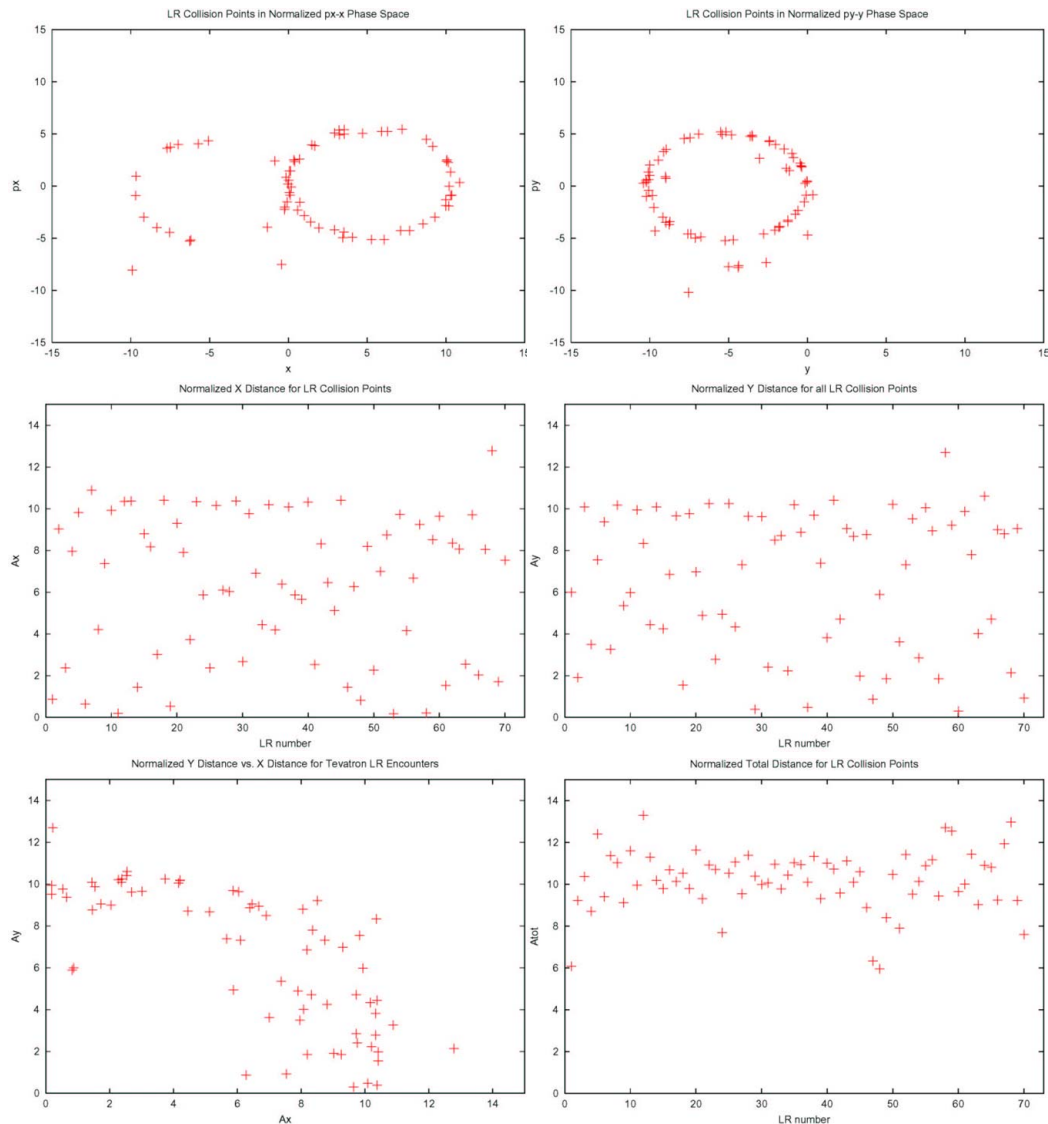


Figure 10: Long-range collisions mapped into normalized phase space at starting point (top row), the normalized horizontal and vertical distance to the other beam at each LR collision point (center row), the two transverse distances plotted against each other (bottom left), and the total distance as a function of encounter number (bottom right).

Figure 11 demonstrates that the closest 3 encounters dominate the 6σ tune footprint (left); the others contribute a negligible spread (right picture). Figure 12 shows tune footprints with all long-range encounters for three bunches in the train: A1, A6 and A12, without and with the two head-on collisions included. The footprints from the long-range collisions alone significantly differ between bunches. The difference is less visible, if the head-on collisions are included.

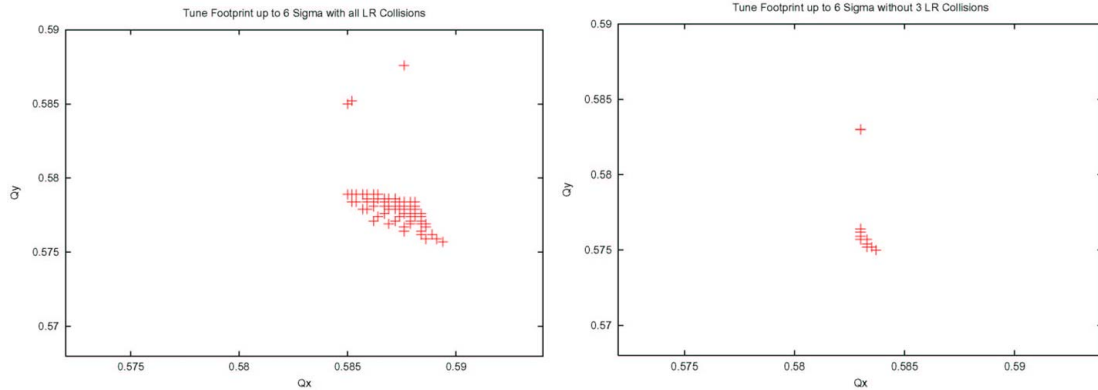


Figure 11: Tune footprint for start amplitudes up to 6σ in each plane with all LR encounters present (left) and without the 3 closest (right) for A6 in collision. Head-on collisions are not included.

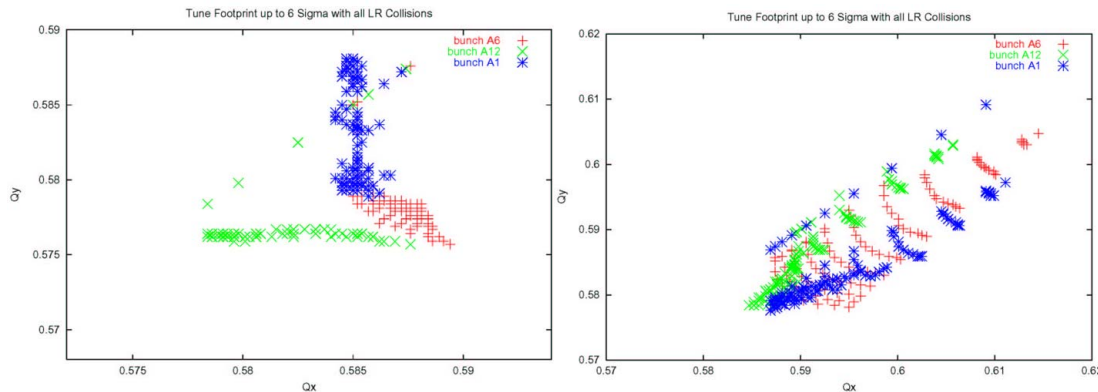


Figure 12: Tune footprints in collision for bunches A1, A6 and A12 with all long-range but no head-on collisions (left) and with long-range plus head-on collisions (right).

Figures 13 and 14 show the transverse diffusion as a function of start amplitude obtained when either all long-range collisions are included, or when the three closest (the only three at distances below 7σ) are removed. The dynamic aperture with all long-range collisions is about 8σ in both planes (Fig. 13). It increases by about 0.7σ , or 10%, when the 3 closest collisions are removed (Fig. 14). However, if we conversely remove all the other collisions and only keep the 3 closest, the dynamic aperture increases by 1.4σ or about 20%, and, in addition, the maximum diffusion speed is much smaller. This is illustrated in Fig. 15. Therefore, the combined effect of all the collisions that are further away on the dynamic aperture is stronger than that of the 3 closest. But removing either part improves the dynamic aperture.

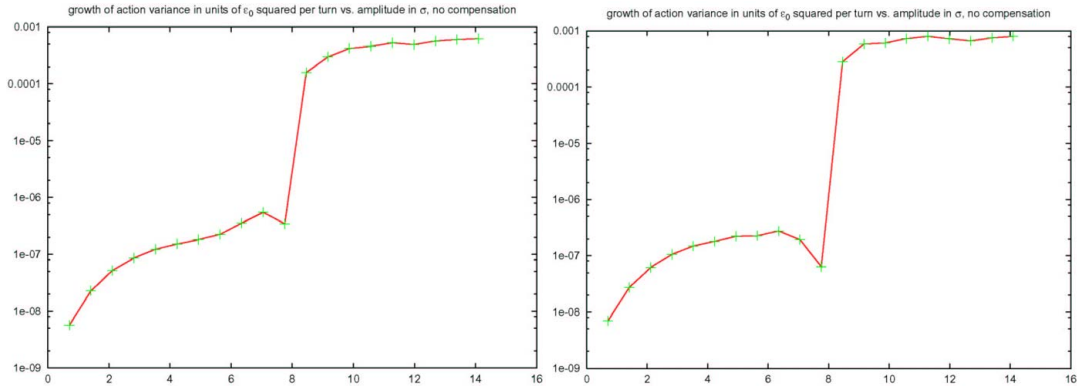


Figure 13: Slope of increase in horizontal (left) and vertical action variance (right) with time in units of the square of the nominal beam emittance per turn as a function of horizontal or vertical start amplitude in units of σ (the start amplitudes in the two planes are chosen equal), for bunch A6 in collision with all long-range collisions.

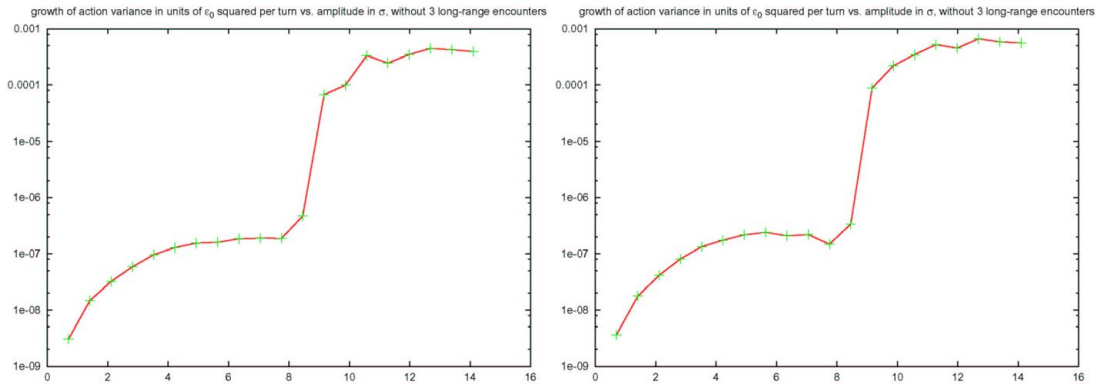


Figure 14: Slope of increase in horizontal (left) and vertical action variance (right) with time in units of the square of the nominal beam emittance per turn as a function of horizontal or vertical start amplitude in units of σ (the start amplitudes in the two planes are chosen equal), for bunch A6 in collision without the 3 closest long-range encounters.

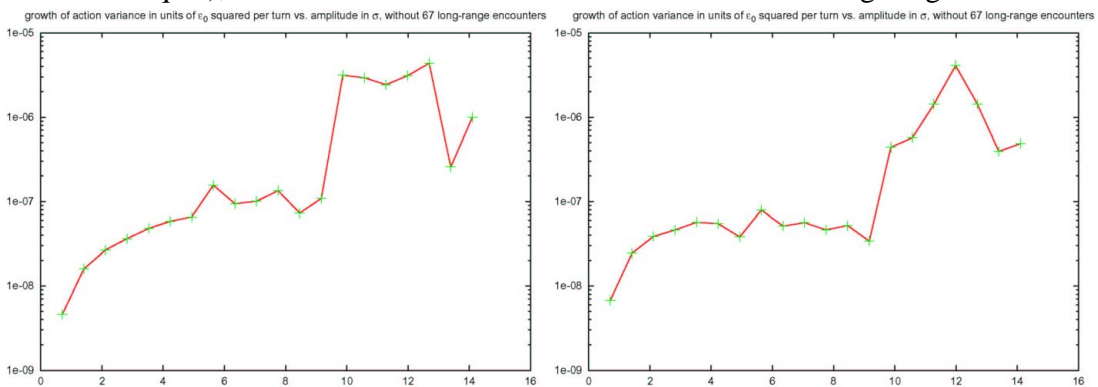


Figure 15: Slope of increase in horizontal (left) and vertical action variance (right) with time in units of the square of the nominal beam emittance per turn as a function of horizontal or vertical start amplitude in units of σ (the start amplitudes in the two planes are chosen equal), for bunch A6 in collision with only the 3 closest and without the 67 other long-range encounters.

Figures 16 and 17 show the diffusion rates computed for bunches A1 and A12 with all long-range collisions included, again without head-on collisions. In both cases the dynamic aperture is much smaller than for bunch A6: bunch A1 has a dynamic aperture of about 6σ and bunch A12 of only 5σ , compared with 8σ for A6.

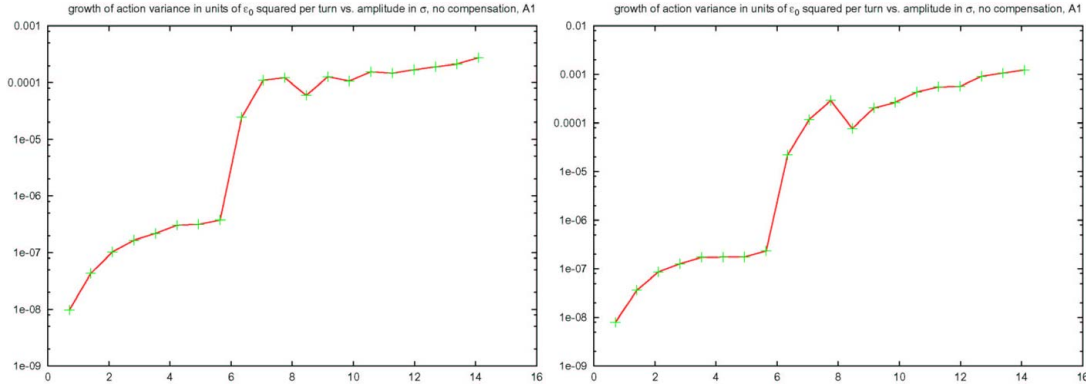


Figure 16: Slope of increase in horizontal (left) and vertical action variance (right) with time in units of the square of the nominal beam emittance per turn as a function of horizontal or vertical start amplitude in units of σ (the start amplitudes in the two planes are chosen equal), for bunch A1 in collision with all long-range encounters.

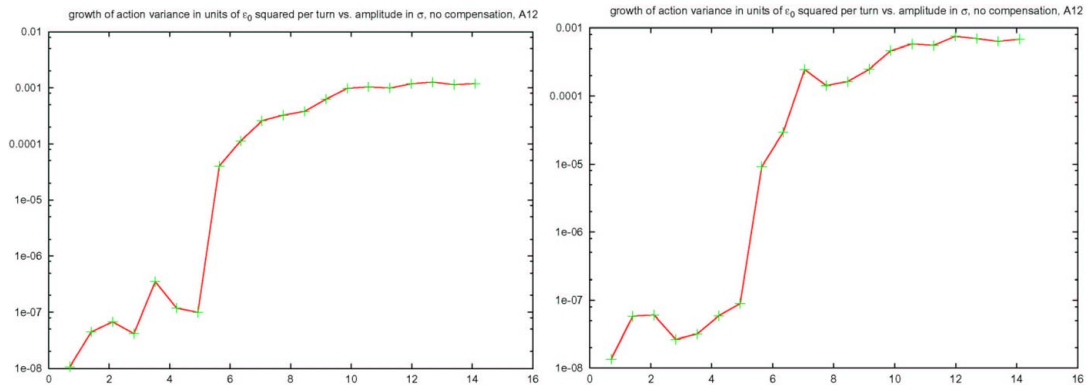


Figure 17: Slope of increase in horizontal (left) and vertical action variance (right) with time in units of the square of the nominal beam emittance per turn as a function of horizontal or vertical start amplitude in units of σ (the start amplitudes in the two planes are chosen equal), for bunch A12 in collision with all long-range encounters.

We now study how much the dynamic aperture changes when the head-on collisions are also included and whether the relative aperture for bunches A1, A6, and A12 would be modified in this case. This is motivated by the notion that our result without head-on collisions possibly is not in accordance with the observed ‘scallop’ [5] (though this is not entirely clear, as bunches with a larger dynamic aperture have more ‘space to blow up’). Figures 18 to 20 present the results for the same three bunches. The diffusive aperture for A1 drops by a remarkable 2σ , due to the addition of the head-on collisions, while those of bunch A6 and A12 decrease little or stay about constant. Hence, the general trend that the center bunches have the largest dynamic aperture remains even in the presence of the head-on collisions. It actually seems to become more pronounced.

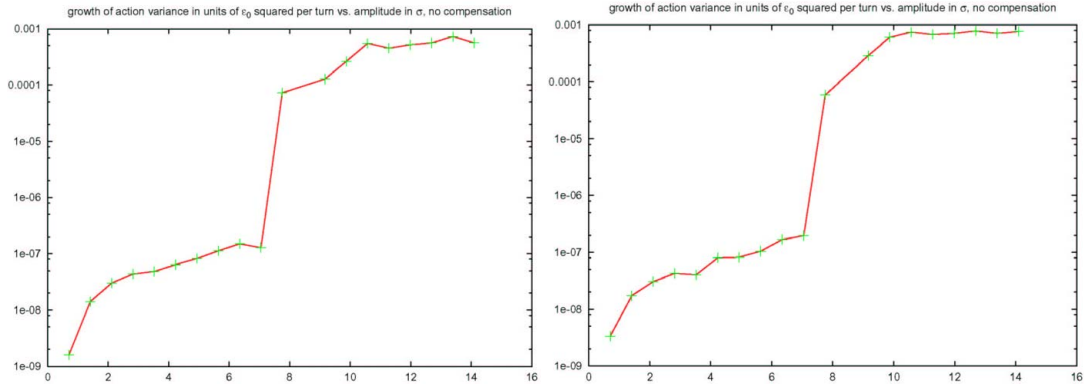


Figure 18: Slope of increase in horizontal (left) and vertical action variance (right) with time in units of the square of the nominal beam emittance per turn as a function of horizontal or vertical start amplitude in units of σ (the start amplitudes in the two planes are chosen equal), for bunch A6 in collision with long-range and two head-on encounters.

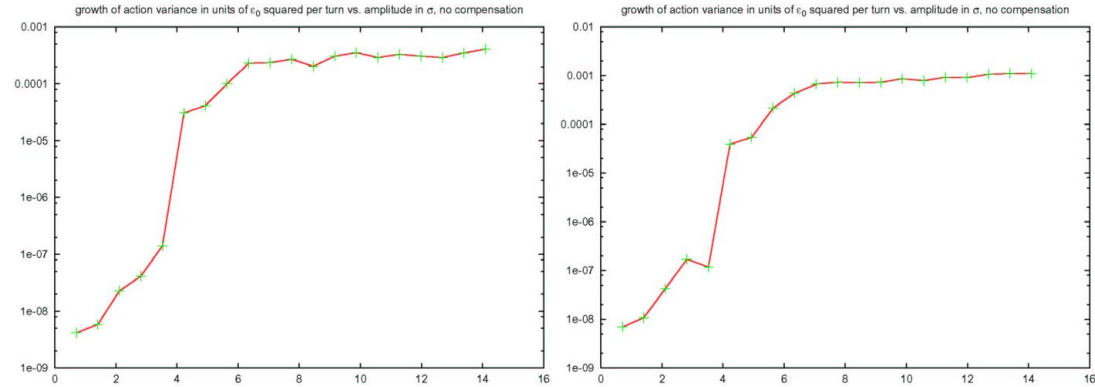


Figure 19: Slope of increase in horizontal (left) and vertical action variance (right) with time in units of the square of the nominal beam emittance per turn as a function of horizontal or vertical start amplitude in units of σ (the start amplitudes in the two planes are chosen equal), for bunch A1 in collision with long-range and two head-on encounters.

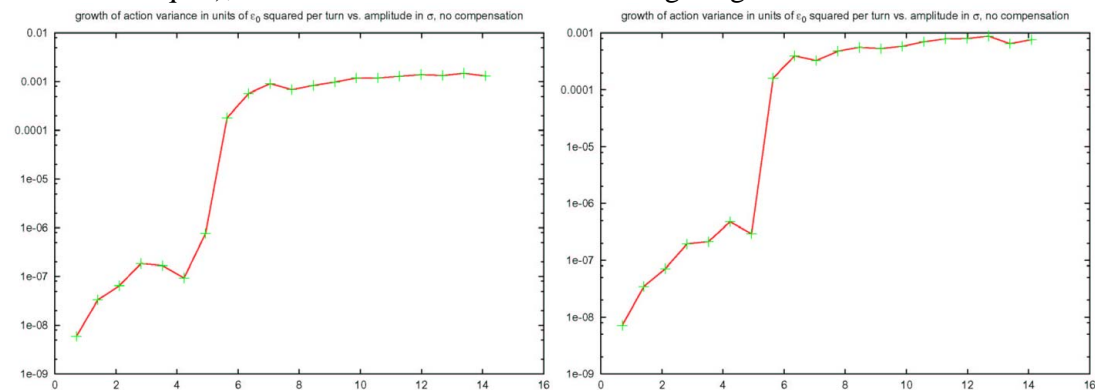


Figure 20: Slope of increase in horizontal (left) and vertical action variance (right) with time in units of the square of the nominal beam emittance per turn as a function of horizontal or vertical start amplitude in units of σ (the start amplitudes in the two planes are chosen equal), for A12 in collision with long-range and two head-on encounters.

Figures 21-26 depict analytical computations, using the formulae of the appendix, for the build-up of tune shifts, chromaticities, coupling, and chromatic coupling around the ring. As usual we compare the three bunches A1, A6 and A12. There are large step-like increases in the vicinity of the two main collision points, and the differences between bunches are significant. Large values are in particular experienced, in some cases, for chromaticity and chromatic coupling. The total effects, accumulated over one turn, are compiled in Table 7. This table confirms the impression that the total tune shifts, chromaticities and chromatic couplings substantially vary from bunch to bunch. To give examples of the most striking dependencies: the induced horizontal chromaticity for bunch A6 is close to 17 units, the vertical for bunch A1 is -7 units, and the real and imaginary part of the chromatic coupling for the latter is about -3 and +4 units.

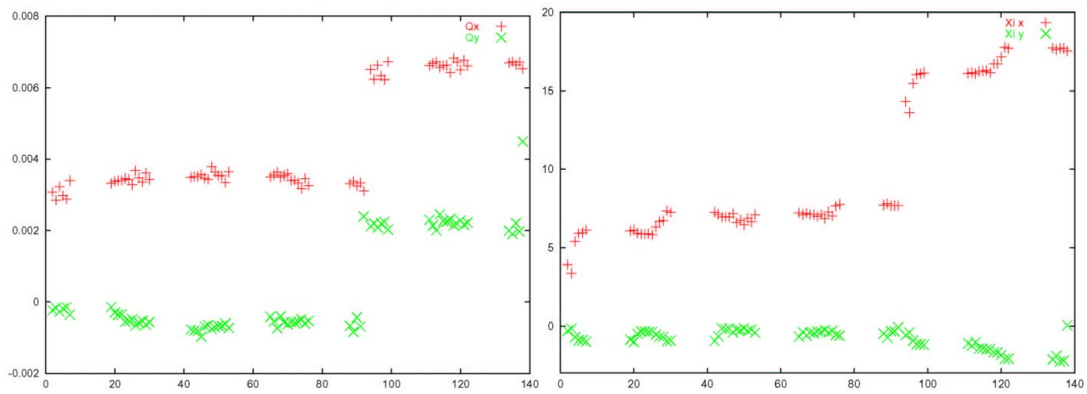


Figure 21: Accumulated horizontal and vertical tune shifts (left) and chromaticities (right) as a function of long-range collision index for bunch A6 in collision.

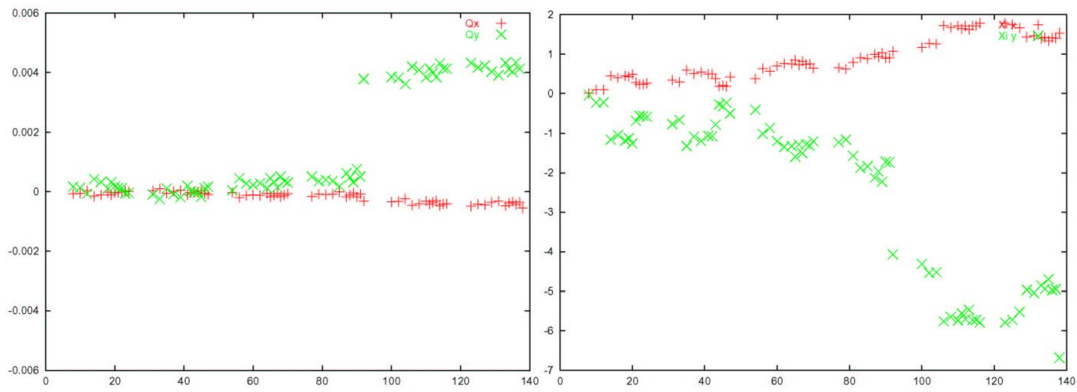


Figure 22: Accumulated horizontal and vertical tune shifts (left) and chromaticities (right) as a function of long-range collision index for bunch A12 in collision.

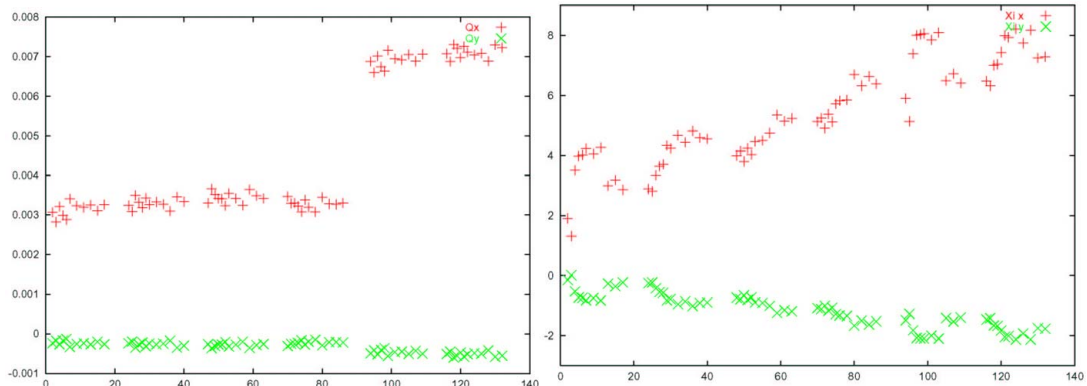


Figure 23: Accumulated horizontal and vertical tune shifts (left) and chromaticities (right) as a function of long-range collision index for bunch A1 in collision

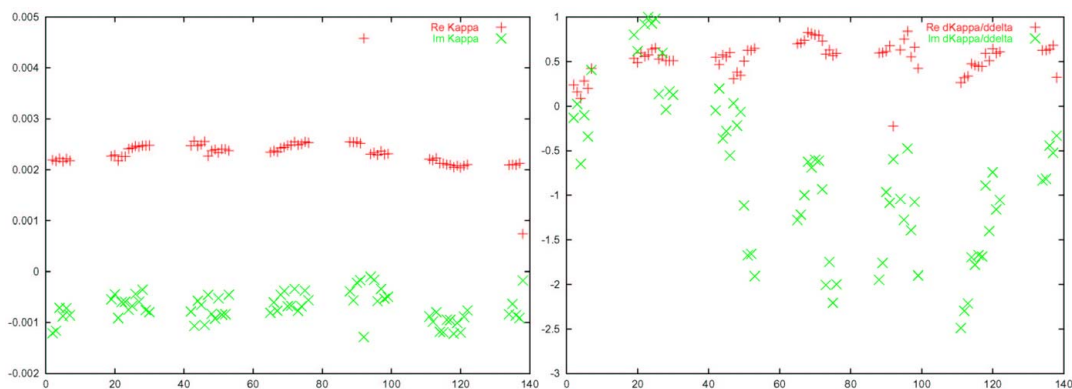


Figure 24: Accumulated real and imaginary coupling components (left) and the chromatic coupling (right) as a function of long-range collision index for bunch A6 in collision.

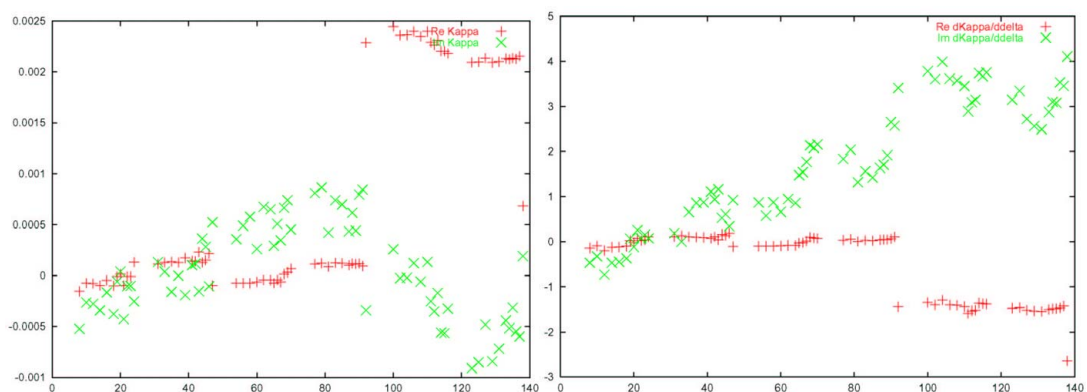


Figure 25: Accumulated real and imaginary coupling components (left) and the chromatic coupling (right) as a function of long-range collision index for bunch A12 in collision.

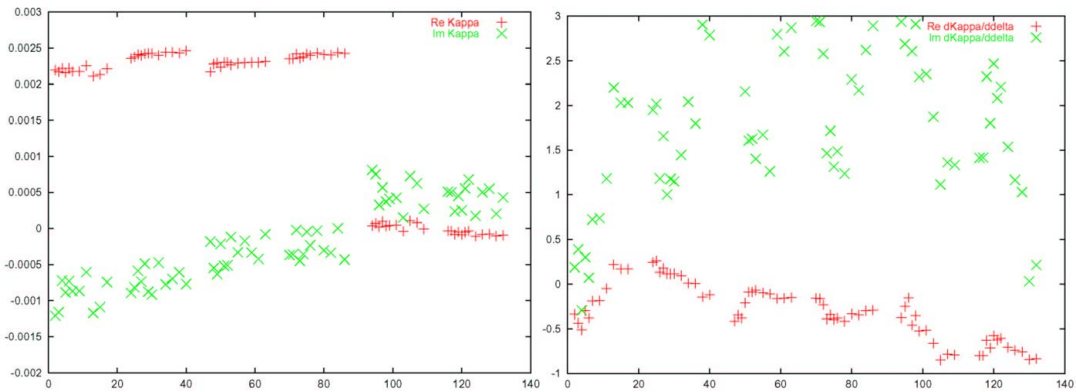


Figure 26: Accumulated real and imaginary coupling components (left) and the chromatic coupling (right) as a function of long-range collision index for bunch A1 in collision.

Table 7: Total tune shifts, chromaticities, coupling driving terms, and chromatic couplings induced by long-range collisions for various pbar bunches in collision.

Pbar bunch	A12	A6	A1
X Tune shift ΔQ_x	-0.00056	0.0065	0.0073
Y Tune shift ΔQ_y	0.0068	0.0045	-0.0006
X Chromaticity Q'_x	1.54	17.52	7.50
Y Chromaticity Q'_y	-6.69	0.042	-2.01
Coupling real part $\text{Re}[\kappa]$	0.00068	0.00075	-0.00010
Coupling imaginary part $\text{Im}[\kappa]$	0.00019	-0.00017	0.00043
Chromatic coupling $\text{Re}[d\kappa/d\delta]$	-2.64	0.32	-0.84
Chromatic coupling $\text{Im}[d\kappa/d\delta]$	4.11	-0.33	0.21

In view of the large values for the chromatic functions, momentum dependence was introduced in the simulation. We can then compute tune footprints time for different constant momentum offsets, also including a nonzero value for the lattice chromaticity (which is modeled by an additional rotation matrix applied once per turn). Figure 27 demonstrates how the momentum dependence widens the footprint.

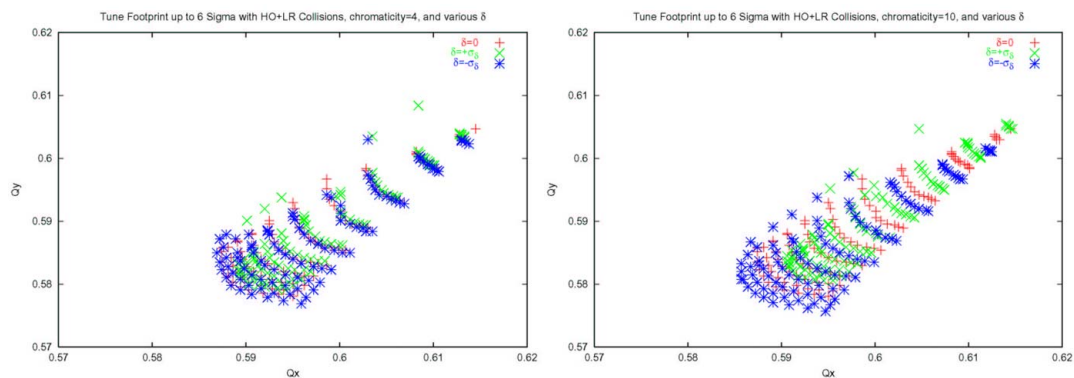


Figure 27: Tune footprints in collision for bunch A6 with all long-range and head-on collisions and three different constant momentum deviations $\delta = -\sigma_\delta, 0, +\sigma_\delta$, for $Q'_{x,y}=4$ (left) and $Q'_{x,y}=10$ (right).

Figures 28 and 29 show diffusion rates computed for A6 with a constant momentum offset equal to $\pm\sigma_\delta$, and including 10 units of lattice chromaticity. The dynamic aperture decreases by about 1σ with respect to the on-momentum case, to $6.3\text{-}7.0\sigma$.

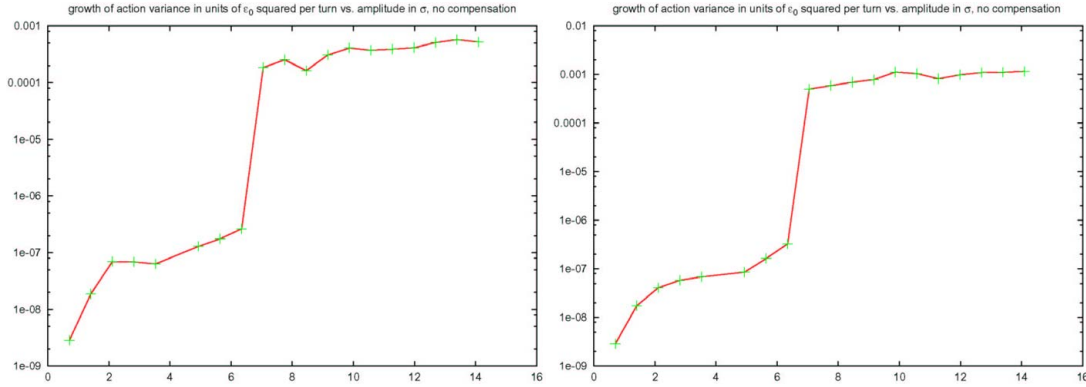


Figure 28: Slope of increase in horizontal (left) and vertical action variance (right) with time in units of the square of the nominal beam emittance per turn as a function of horizontal or vertical start amplitude in units of σ (the start amplitudes in the two planes are chosen equal), for bunch A6 in collision with long-range and two head-on encounters, with a chromaticity $Q'_{x,y}=10$ and $\delta=+\sigma_\delta$.

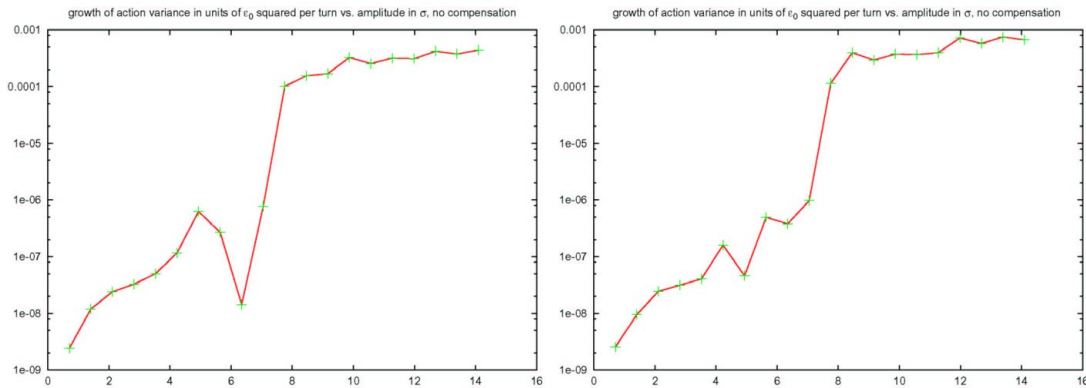


Figure 29: Slope of increase in horizontal (left) and vertical action variance (right) with time in units of the square of the nominal beam emittance per turn as a function of horizontal or vertical start amplitude in units of σ (the start amplitudes in the two planes are chosen equal), for bunch A6 in collision with long-range and two head-on encounters, with a chromaticity $Q'_{x,y}=10$ and $\delta=-\sigma_\delta$.

Conclusions

Weak-strong beam-beam simulations with various numbers of long-range encounters were performed for antiproton bunch A1 at injection (cogging '0' stat) and for A1, A6 and A12 at top energy. For injection, the effect of 4 wires with parameters previously computed by B. Erdelyi was also investigated, in the presence of long-range collisions only (Erdelyi's study also included lattice errors). For these studies the code WSDIFF

was significantly modified so as to model an arbitrary number of different long-range collisions with varying beam sizes and transverse distances in two transverse dimensions plus several wires, where all nonlinear elements are connected by the linear transport-matrices read from the up-to-date optics. The extended WSDIFF code also includes momentum offsets the dispersion at the long-range encounters, and a nonzero chromaticity. WSDIFF was benchmarked against the FNAL code BBSIM; similar tune footprints were obtained by both programs. Most of the simulations were performed for an on-energy particle in 4D. Only a few preliminary results illustrate the dependence on momentum. Mapping the position of the long-range encounters to the same location in normalized phase space reveals a peculiar helix and double-helix structure for the two planes. The plane of the double helix changes from the vertical to the horizontal direction in going from injection to top energy. There is a preferred orientation of the long-range encounters, which may suggest that the compensating wires should be placed with roughly the same orientation.

A main finding of the simulation is that the solution of 4 wires at injection, previously determined by B. Erdelyi, indeed raises the dynamic aperture seen in the vertical diffusion, namely from about 4.5σ to 6σ , by about 1.5σ (the dynamic aperture inferred from the horizontal diffusion stays constant at about 6σ). Eliminating the 6 closest long-range encounters at injection has a smaller effect on the aperture.

At top energy, three collisions are much closer than the rest, for a typical bunch in the train (A6). Removing these three collisions increases the dynamic aperture for A6 from 8σ to 8.7σ . But removing instead the 67 other collisions, increases the aperture from 8σ to 9.4σ , which shows that the many other collisions are important, despite of being about 2σ further away and despite of the fact that the 3 closest completely dominate the tune footprint up to 6σ . Hence, as previously noted by T. Sen and others, there is little correlation between tune footprint and dynamic aperture.

With all long-range encounters present, the dynamic aperture is 8σ for bunch A6, 6σ for A1 and only 5σ for A12. This great variation suggests that it may be difficult to find a wire setting that is beneficial for all bunches. Nonetheless since bunches A2 to A11 occupy approximately the same region in tune space, it may be possible to compensate these ten bunches, though not the two outliers A1 and A12. The pattern of different dynamic apertures for bunches A1, A6 and A12 stays intact when the head-on collisions are included; it even gets slightly more pronounced. This simulation result that A1 and A12 have a smaller diffusive aperture than A6, when all long-range and head-on collisions are included, is probably in contradiction with the "scallop" that are observed during Tevatron operation. The smaller dynamic aperture of A1 and A12 could explain these scallops, if it led to a shaving of A1 and A12 and, thereby, bounded their emittance. This scenario would also imply that A1 and A12 suffer a larger intensity loss than the other bunches, when the scallops appear, which, likely, is not the case. The majority of the stores do not develop scallops, however. For these typical cases we might expect to see larger losses in A1 and A12, if the dynamic aperture of these bunches is reduced in accordance with the simulation. The dynamic losses caused by the long-range collisions could be inferred from the bunch-current evolution after subtracting contributions from other sources, e.g., luminosity, which are independent of the dynamic aperture.

Finally, analytical calculations show that at collision energy the differences in tune shifts due to the different long-range encounters are of the order 0.007 in both planes, the

differences in horizontal chromaticity 16 units horizontally and 7 units vertically, in coupling about 0.0004-0.0006, and in chromatic coupling about 3-5 units. This indicates that, in particular, the chromatic effects will be different from bunch to bunch. For this reason, the momentum dependence was included in the code. We find that at an offset of $1\sigma_\delta$ the diffusive aperture is reduced by about 1σ from the on-momentum case.

Table 8 presents a summary of the dynamic apertures simulated under various conditions.

Table 8: Dynamic aperture in units of σ found for various cases by simulation.

case	bunch	condition	horizontal	vertical
injection	A1	all long-range	6.0	4.5
		w/o 6 closest	6.0	5.0
		all long-range & 4 wires	6.0	6.0
collision	A6	all long-range	8.0	8.0
		w/o 3 closest	8.7	8.7
		w/o 67 others	9.4	9.4
		all long-range plus head on	7.4	7.4
		all long-range plus head on, $Q'_{x,y}=10, \delta=\sigma_\delta$	6.3	6.3
		all long-range plus head on, $Q'_{x,y}=10, \delta=-\sigma_\delta$	6.3	7.0
		A1	all long-range	6.0
		all long-range plus head-on	4.0	4.0
	A12	all long-range	5.0	5.0
		all long-range plus head-on	4.5	5.0

The appendix compiles analytical expressions for various quantities. An analytical solution for the diffusion coefficient in 4D has so far eluded the capabilities of Mathematica.

Acknowledgements

F.Z. thanks T. Sen and V. Shiltsev for inviting him to Fermilab and J.-P. Koutchouk for initiating this collaboration. He would like to thank all of them, as well as B. Erdelyi, P. Lebrun, X.-L. Zhang, P. Bauer, K. Desler, and K. Seiya for their generous hospitality, for many inspiring discussions, for much helpful information, and for providing the unique possibility to participate in a TEL machine experiment. M. Kriss and S. Jarocki provided indispensable computing assistance. We thank S. Holmes, J.-P. Riunaud and F. Ruggiero for supporting this activity.

References

- [1] P. Lebrun, T. Sen, V. Shiltsev, X.-L. Zhang, F. Zimmermann, "Using the Electron Lens as a Wire and Other TEL Studies", report in preparation (2004).
- [2] T. Sen, B. Erdelyi, M. Xiao, V. Boochoa, "Beam-Beam Effects at the Tevatron: Theory", submitted to Phys. Rev. ST Accel. Beams (2004).
- [3] Y. Papaphilippou, F. Zimmermann, "Weak-Strong Beam-Beam Simulations for the Large Hadron Collider," Phys. Rev. ST Accel. Beams 2, 104001 (1999).
- [4] B. Erdelyi, "Wire Compensation Studies," FNAL Review of Wire-Based Beam-Beam Compensation, October 6, 2003.
- [5] V. Shiltsev, private communication (2004).

Appendix: Analytical Expressions

Tune Shift and Coupling

The horizontal and vertical deflections of a single particle at a parasitic collision point are

$$\Delta x' = -\frac{2N_b r_p (d_x + x)}{\gamma((d_x + x)^2 + (y + d_y)^2)} + \frac{2N_b r_p d_x}{\gamma(d_x^2 + d_y^2)} \equiv -C \left[\frac{d_x + x}{(d_x + x)^2 + (d_y + y)^2} - \frac{d_x}{d_x^2 + d_y^2} \right]$$

$$\Delta y' = -\frac{2N_b r_p (d_y + y)}{\gamma((d_x + x)^2 + (d_y + y)^2)} + \frac{2N_b r_p d_y}{\gamma(d_x^2 + d_y^2)} \equiv -C \left[\frac{d_y + y}{(d_x + x)^2 + (d_y + y)^2} - \frac{d_y}{d_x^2 + d_y^2} \right]$$

where d_x and d_y denote the transverse position of the center of the other beam, and $C \equiv 2N_b r_p / \gamma$. Differentiating these expressions and evaluating them at zero yields the terms responsible for a linear tune shift and linear coupling:

$$\left. \frac{\partial \Delta x'}{\partial x} \right|_{x=y=0} = -C \frac{1}{d^2} \left(1 - 2 \frac{d_x^2}{d^2} \right) \quad \left. \frac{\partial \Delta x'}{\partial y} \right|_{x=y=0} = 2C \frac{d_x d_y}{d^4}$$

$$\left. \frac{\partial \Delta y'}{\partial y} \right|_{x=y=0} = -C \frac{1}{d^2} \left(1 - 2 \frac{d_y^2}{d^2} \right) \quad \left. \frac{\partial \Delta y'}{\partial x} \right|_{x=y=0} = 2C \frac{d_x d_y}{d^4}$$

We can identify the integrated quadrupole and skew quadrupole strengths as

$$K_{n;x} = \frac{2N_b r_p}{\gamma d^2} \left(\frac{d_y^2 - d_x^2}{d^2} \right), \quad K_s = -\frac{4N_b r_p}{\gamma d^2} \frac{d_x d_y}{d^2}$$

From this, the total coupling driving terms is obtained by summing over all collisions with the appropriate beta-function and phase weights:

$$|\kappa_-| = \frac{1}{2\pi} \left| \sum_k K_s \sqrt{\beta_x \beta_y} e^{i(\phi_x - \phi_y - (Q_x - Q_y - q)2\pi s/L)} \right|$$

and in first order and linear approximation the tune shift is

$$\Delta Q_{x,y} = \frac{1}{4\pi} \sum K_{n;x,y} \beta_{x,y},$$

where $K_{n;y} = -K_{n;x}$.

Chromaticity and Skew Chromaticity

Let us now also introduce dispersion at the long-range collision points. The deflection experienced by a particle becomes

$$\Delta x' = -\frac{2N_b r_p (d_x + D_x \delta + x)}{\gamma((d_x + D_x \delta + x)^2 + (y + D_y \delta + d_y)^2)} + \frac{2N_b r_p d_x}{\gamma(d_x^2 + d_y^2)} \equiv -C \left[\frac{d_x + D_x \delta + x}{(d_x + D_x \delta + x)^2 + (d_y + D_y \delta + y)^2} - \frac{d_x}{d_x^2 + d_y^2} \right]$$

$$\Delta y' = -\frac{2N_b r_p (d_y + D_y \delta + y)}{\gamma((d_x + D_x \delta + x)^2 + (d_y + D_y \delta + y)^2)} + \frac{2N_b r_p d_y}{\gamma(d_x^2 + d_y^2)} \equiv -C \left[\frac{d_y + D_y \delta + y}{(d_x + D_x \delta + x)^2 + (d_y + D_y \delta + y)^2} - \frac{d_y}{d_x^2 + d_y^2} \right]$$

As before differentiating with respect to the transverse coordinates gives quadrupole and skew-quadrupole components, which now, via the dispersion (and also via the natural chromaticity due to the momentum-dependence of γ), depend on the momentum deviation.

$$\left. \frac{\partial \Delta x'}{\partial x} \right|_{x=y=0} = - \left. \frac{\partial \Delta y'}{\partial y} \right|_{x=y=0} = - \frac{C}{1-\delta} \frac{1}{(d_x + D_x \delta)^2 + (d_y + D_y \delta)^2} \left(1 - 2 \frac{(d_x + D_x \delta)^2}{(d_x + D_x \delta)^2 + (d_y + D_y \delta)^2} \right)$$

$$\left. \frac{\partial \Delta x'}{\partial y} \right|_{x=y=0} = \left. \frac{\partial \Delta x'}{\partial x} \right|_{x=y=0} = 2 \frac{C}{1-\delta} \frac{(d_x + D_x \delta)(d_y + D_y \delta)}{[(d_x + D_x \delta)^2 + (d_y + D_y \delta)^2]}$$

The first order chromaticity is

$$Q_x' = - \frac{C}{4\pi} \sum_k \left[\frac{d_x^4 - 2d_x^3 D_x + 6d_x D_x d_y^2 - d_y^4 + 2d_y^3 D_y - 6d_x^2 d_y D_y}{d^6} \right] \beta_k$$

$$Q_y' = \frac{C}{4\pi} \sum_k \left[\frac{d_x^4 - 2d_x^3 D_x + 6d_x D_x d_y^2 - d_y^4 + 2d_y^3 D_y - 6d_x^2 d_y D_y}{d^6} \right] \beta_y$$

$$\frac{d\kappa}{d\delta} = - \frac{C}{\pi} \sum_k \frac{-3d_x^2 D_x d_y + D_x d_y^3 + d_x d_y^2 (d_y - 3D_y) + d_x^3 (d_y + D_y)}{(d_x^2 + d_y^2)^3} \sqrt{\beta_x \beta_y} e^{i(\phi_x - \phi_y - (Q_x - Q_y - q)2\pi/L)}$$

Diffusion Coefficient

The change in action due to the long-range beam-beam kick is

$\Delta J_x = \alpha_x x \Delta x' + \beta_x x' \Delta x' + \beta_x (\Delta x')^2 \approx \alpha_x x \Delta x' + \beta_x x' \Delta x' = \sqrt{2J_x \beta_x} \cos \phi \Delta x'$, and an analogous expression holds for the vertical plane.

$$\Delta J_x = -\sqrt{2J_x \beta_x} \cos \phi_x C \left[\frac{d_x + \sqrt{2J_x \beta_x} \sin \phi_x}{(d_x + \sqrt{2J_x \beta_x} \sin \phi_x)^2 + (d_y + \sqrt{2J_y \beta_y} \sin \phi_y)^2} - \frac{d_x}{d_x^2 + d_y^2} \right]$$

Introducing the abbreviations

$$A_x \equiv \frac{\sqrt{2J_x \beta_x}}{d_x}, \quad A_y \equiv \frac{\sqrt{2J_y \beta_y}}{d_y}, \quad \kappa \equiv \frac{d_y}{d_x},$$

this can be rewritten as

$$\Delta J_x = -CA_x \cos \phi_x \left[\frac{1 + A_x \sin \phi_x}{(1 + A_x \sin \phi_x)^2 + \kappa^2 (1 + A_y \sin \phi_y)^2} - \frac{1}{1 + \kappa^2} \right]$$

$$= -CA_x \cos \phi_x \left[\frac{-A_x \sin \phi_x + \kappa^2 A_x \sin \phi_x + A_x^2 \sin^2 \phi_x - 2\kappa^2 A_y \sin \phi_y - \kappa^2 A_y^2 \sin^2 \phi_y}{[(1 + A_x \sin \phi_x)^2 + \kappa^2 (1 + A_y \sin \phi_y)^2] (1 + \kappa^2)} \right]$$

Similarly we have for the vertical plane

$$\Delta J_y = -CA_y \cos \phi_y \left[\frac{1 + A_y \sin \phi_y}{(1 + A_y \sin \phi_y)^2 + \kappa^{-2} (1 + A_x \sin \phi_x)^2} - \frac{1}{1 + \kappa^{-2}} \right]$$

$$= -CA_y \cos \phi_y \left[\frac{-A_y \sin \phi_y + \kappa^{-2} A_y \sin \phi_y + A_y^2 \sin^2 \phi_y - 2\kappa^{-2} A_x \sin \phi_x - \kappa^{-2} A_x^2 \sin^2 \phi_x}{[(1 + A_y \sin \phi_y)^2 + \kappa^{-2} (1 + A_x \sin \phi_x)^2] (1 + \kappa^{-2})} \right]$$

Assuming complete phase randomization, in the chaotic sea outside of the dynamic aperture the diffusion coefficient can be estimated as

$$D(J_{x,y}) \approx \frac{1}{8\pi^2} \int_0^{2\pi} \int_0^{2\pi} (\Delta J_{x,y})^2 d\phi_x d\phi_y.$$